

Internal Control of Hurricane Intensity Variability: The Dual Nature of Potential Vorticity Mixing

CHRISTOPHER M. ROZOFF AND JAMES P. KOSSIN

University of Wisconsin—Madison, Madison, Wisconsin

WAYNE H. SCHUBERT

Colorado State University, Fort Collins, Colorado

PEDRO J. MULERO

University of Wisconsin—Madison, Madison, Wisconsin

(Manuscript received 18 December 2007, in final form 9 June 2008)

ABSTRACT

In hurricane eyewalls, the vertical stretching effect tends to produce an annular ring of high vorticity. Idealized, unforced nondivergent barotropic model results have suggested such rings of vorticity are often barotropically unstable, leading to strong asymmetric mixing events where vorticity is mixed inward into a more stable configuration. Such mixing events most often result in weakened maximum winds. The manner in which forcing modifies these unforced simulations remains an open question.

In the current study, a forced, two-dimensional barotropic model is used to systematically study the sensitivity of vorticity rings to ring geometry and spatially and temporally varying forcing. The simulations reveal an internal mechanism that interrupts the intensification process resulting from vorticity generation in the hurricane eyewall. This internal control mechanism is due to vorticity mixing in the region of the eye and eyewall and can manifest itself in two antithetical forms—as a transient “intensification brake” during symmetric intensification or as an enhancer of intensification through efficient transport of vorticity from the eyewall, where it is generated, to the eye.

1. Introduction

Hurricane intensity change is governed by a number of known factors. The climatology of intensity change was documented by Dvorak (1984), who showed that an average tropical storm intensifies at a rate of a few meters per second per day, and an average hurricane¹ intensifies at a rate of approximately 12–13 m s⁻¹ day⁻¹. This mean intensity change typically continues for 3–5 days after attainment of tropical storm strength (18 m s⁻¹). After maximum intensity, weakening typi-

cally occurs at a slower rate. This was recently corroborated and extended by Emanuel (2000), who showed that a storm that does not encounter land or decreasing sea surface temperatures intensifies—on average—at a rate of approximately 12 m s⁻¹ day⁻¹ for about 5 days, followed by weakening at a slower rate of about 8 m s⁻¹ day⁻¹.

Among the factors determining the climatology of intensity change, it is well known that environmental conditions play a key role (e.g., Gray 1968; Merrill 1988; DeMaria and Kaplan 1994; Dunion and Velden 2004; Emanuel et al. 2004). For example, if a storm moves over land or into regions of colder water, lower ocean heat content, reduced relative humidity, or strong ambient vertical wind shear, weakening often follows. Alternatively, an environment that is not conducive for intensification can become more favorable over time. Ideally, then, the variance of hurricane intensity change from climatology would be explained in terms of the variance of the synoptic-scale storm envi-

¹ For simplicity, we use the term “hurricane” to mean a tropical cyclone in any oceanic basin.

Corresponding author address: Christopher M. Rozoff, CIMSS, University of Wisconsin—Madison, 1225 West Dayton Street, Madison, WI 53706.
E-mail: chris.rozoff@ssec.wisc.edu

ronment. This is not the case, however, and it is fairly typical for storms to strengthen or weaken, sometimes rapidly, without any clear commensurate changes in the storm environment. Although the specific processes involved remain an open question, this behavior is widely believed to result from internal mesoscale processes that can have a profound effect on how storm intensity evolves. This implies that the ability to model and ultimately predict hurricane intensity change is dependent on the capability to contemporaneously model a very broad range of spatial scales.

From a more immediately pragmatic viewpoint, it is revealing to note that our operational ability to accurately forecast hurricane motion (track) has improved dramatically in the past 20 yr and that the reason for this lies in our improving ability to capture evolving synoptic-scale fields with our present numerical guidance. With the exception of occasional small-amplitude trochoidal oscillations (e.g., Muramatsu 1986; Nolan et al. 2001), which are on the order of tens of kilometers and are caused by transient potential vorticity (PV) asymmetries near the storm center, the track is controlled almost entirely by the environmental steering flow in which the storm vortex is embedded. Contrary to track forecasting, our ability to forecast intensity change has shown almost no progress in the past 20 yr, which is believed to be due to our present inability to adequately model internal processes in hurricanes.

A full description of the intricate moist physical processes occurring in hurricanes requires a three-dimensional (3D), nonhydrostatic model that includes prediction equations for the amounts of the various categories of condensed water substance. Such “full-physics” models are capable of simulating both the nonhydrostatic dynamics of individual cumulonimbus clouds and the larger-scale, quasi-static, quasi-balanced dynamics of the hurricane vortex. Like most large-scale dynamical phenomena in geophysical fluid dynamics, the hurricane vortex can be understood in terms of its PV dynamics. However, unlike the case of midlatitude baroclinic waves, for which material conservation of PV on short time scales is a valid approximation, the PV dynamics of hurricanes involves diabatic and frictional sources and sinks in a fundamental way. Recently, Schubert et al. (2001) and Schubert (2004) derived a PV principle for the full-physics model developed by Ooyama (1990, 2001). Neglecting those precipitation effects that tend to be of secondary importance, this PV principle takes the form

$$\frac{DP}{Dt} = \frac{1}{\rho} \boldsymbol{\zeta} \cdot \nabla \dot{\theta}_\rho + \frac{1}{\rho} (\nabla \times \mathbf{F}) \cdot \nabla \theta_\rho, \quad (1)$$

where $P = \rho^{-1} \boldsymbol{\zeta} \cdot \nabla \theta_\rho$ is the PV, $D/Dt = \partial/\partial t + \mathbf{u} \cdot \nabla$ the material derivative, \mathbf{u} the three-dimensional vector velocity of the dry air and the airborne moisture, $\boldsymbol{\zeta} = 2\boldsymbol{\Omega} + \nabla \times \mathbf{u}$ the absolute vorticity vector, ρ the total density (sum of the densities of dry air, water vapor, airborne condensate, and precipitation), θ_ρ the virtual potential temperature, $\dot{\theta}_\rho$ the material rate of change of θ_ρ , and \mathbf{F} the frictional force per unit mass. It should be noted that (1) does not differ greatly from the PV equation for a dry atmosphere because the total density ρ is approximately equal to the dry air density and the virtual potential temperature θ_ρ is approximately equal to the dry potential temperature. Based on (1), we can say that there are three aspects to understanding the PV structure in hurricanes: (i) the advective aspects embodied in the D/Dt operator, (ii) the diabatic source/sink effect $\rho^{-1} \boldsymbol{\zeta} \cdot \nabla \dot{\theta}_\rho$, and (iii) the frictional source/sink effect $\rho^{-1} (\nabla \times \mathbf{F}) \cdot \nabla \theta_\rho$. Although the frictional effect can play an important role, especially in the lowest kilometer, it is the diabatic source/sink that is responsible for the extremely large PV found in the hurricane eyewall region (e.g., Yau et al. 2004; Hausman et al. 2006). The physical interpretation of the $\rho^{-1} \boldsymbol{\zeta} \cdot \nabla \dot{\theta}_\rho$ term is facilitated by rewriting it as

$$\begin{aligned} \frac{1}{\rho} \boldsymbol{\zeta} \cdot \nabla \dot{\theta}_\rho &= \left(\frac{1}{\rho} \boldsymbol{\zeta} \cdot \nabla \theta_\rho \right) \left(\frac{\boldsymbol{\zeta} \cdot \nabla \dot{\theta}_\rho}{\boldsymbol{\zeta} \cdot \nabla \theta_\rho} \right) \\ &= P \left(\frac{\mathbf{k} \cdot \nabla \dot{\theta}_\rho}{\mathbf{k} \cdot \nabla \theta_\rho} \right) \\ &= P \left(\frac{\partial \dot{\theta}_\rho}{\partial \theta_\rho} \right)_\zeta, \end{aligned} \quad (2)$$

where $\mathbf{k} = \boldsymbol{\zeta}/|\boldsymbol{\zeta}|$ is the unit vector pointing along the absolute vorticity vector and where $(\partial/\partial \theta_\rho)_\zeta$ indicates that the partial derivative is taken along the vorticity vector. Using (2) in (1) and neglecting the frictional term, we obtain

$$\frac{\partial P}{\partial t} + \mathbf{u} \cdot \nabla P = P \left(\frac{\partial \dot{\theta}_\rho}{\partial \theta_\rho} \right)_\zeta. \quad (3)$$

If $\dot{\theta}_\rho$ is a maximum at midtropospheric levels, upward-moving air parcels experience an exponential increase in PV in the lower troposphere. Above the heating maximum, the parcels experience a decrease of PV but maintain a positive PV anomaly through a deep layer. In the highly persistent convection in tropical depressions and storms, this process forms a vertically deep tower of positive PV. When an eye forms, PV production occurs in the eyewall, but convection and PV production cease in the eye. This can lead to a vortex structure in which PV is very large in an outwardly sloping

annular region just outside the eye (e.g., Fig. 12 of Yau et al. 2004; Figs. 6 and 10 of Hausman et al. 2006). The dynamic stability of such flows, their nonlinear evolution and mixing properties, and their observational documentation and laboratory simulation have been topics of much recent interest (e.g., Schubert et al. 1999; Kossin et al. 2000; Nolan and Montgomery 2000, 2002; Kossin and Eastin 2001; Kossin and Schubert 2001, 2004; Kossin et al. 2002; Montgomery et al. 2002; Terwey and Montgomery 2002; Wang 2002a,b; Knaff et al. 2003; Nolan and Grasso 2003; Mashiko 2005; Kwon and Frank 2005; Yang et al. 2007).

In uniform and favorable environments for hurricanes, the mixing and asymmetries that result from barotropic instability events can have substantial impacts on the intensity of a mature hurricane. In the idealized studies of Schubert et al. (1999) and Nolan and Montgomery (2002), it was demonstrated that barotropic instability and vorticity mixing can decrease the maximum wind speed. Another way in which barotropic instability can weaken a hurricane was demonstrated in the high-resolution, full-physics hurricane simulations described in Yang et al. (2007). Comparing axisymmetric and 3D hurricane simulations, Yang et al. found that their 3D storm was weaker than the axisymmetric counterpart because of an interesting sequence of events. In particular, PV mixing in the 3D simulation reduced the tilt of the eyewall, leading to downdrafts that were warmer and moister than those underneath the tilted eyewall of their axisymmetric simulation. The weaker downdrafts in the 3D simulation led to a smaller air–sea entropy deficit near the radius of maximum winds, which reduced the energy input into the storm. Alternatively, mesovortices resulting from barotropic instability may also intensify hurricanes by transporting high-entropy air from the eye into the eyewall (e.g., Persing and Montgomery 2003; Cram et al. 2007; Bell and Montgomery 2008). Thus, a range of hurricane models and observations implies that barotropic instability and vorticity mixing can impact hurricane intensity in a number of direct and indirect ways.

The purpose of the present paper is to add to the body of knowledge on barotropic instability by considering the simultaneous effects of forcing and vorticity mixing in a very idealized framework. In particular, we shall be concerned with the interaction of the advective aspects and the diabatic aspects of the PV evolution and seek to elucidate their potential impacts on intensity change. The exact internal processes that govern intensity change are presently unknown, but it is believed that the rearrangement of the inner core PV structure plays an important role. To isolate these aspects of the flow evolution in the simplest dynamical

context and to gain further understanding of these internal governing mechanisms, we will consider the role of two-dimensional (2D) barotropic processes in the hurricane inner core when forcing (diabatic heating and friction) is continuously applied to annular rings representative of hurricane eyewalls. We will use results from a nondivergent barotropic model to explore the range of evolutions for continuously forced annular vorticity rings.

The paper is organized as follows: First, the dynamical equations and forcing are presented in section 2. After specifying the family of forcing functions in section 3, the model is then used in section 4 to simulate a range of eyewall geometries. Results from a series of sensitivity experiments are summarized in section 5. Concluding remarks are presented in section 6.

2. The nondivergent barotropic model with forcing

The physical model used here is the f -plane nondivergent barotropic model, for which the governing equations are

$$\frac{\partial \zeta}{\partial t} - \frac{\partial \psi}{\partial y} \frac{\partial \zeta}{\partial x} + \frac{\partial \psi}{\partial x} \frac{\partial \zeta}{\partial y} = (f + \zeta) \left(1 - \frac{f + \zeta}{f + \zeta_m} \right) C - \mu \zeta + \nu \nabla^2 \zeta \quad \text{and} \quad (4)$$

$$\nabla^2 \psi = \zeta, \quad (5)$$

where ζ is the relative vorticity, ψ the streamfunction, f the constant Coriolis parameter, μ the constant coefficient for Rayleigh friction, ν the constant diffusion coefficient, and ∇^2 the horizontal Laplacian operator. Although the model is nondivergent, we have written the vorticity generation term in a form similar to the divergence term of a more general dynamical model—that is, as the product of the absolute vorticity $f + \zeta$ and the convergence $C(r)$, which is assumed to be a specified function of $r = (x^2 + y^2)^{1/2}$. However, to prevent unlimited growth of the vorticity, the generation term has been “logistically limited” by the factor $1 - (f + \zeta)/(f + \zeta_m)$, where ζ_m is a specified constant with subscript m representing the maximum vorticity achieved (see 10 below) by the generation term. Because the nondivergent model makes no distinction between absolute vorticity and PV, we could interpret the generation term on the right-hand side of (4) as analogous to the forcing term on the right-hand side of (3)—that is, the logistically limited convergence $[1 - (f + \zeta)/(f + \zeta_m)]C$ could be interpreted as analogous to $(\partial \theta_p / \partial \theta_p)_\zeta$. However, the analogy should not be taken too far because (4) describes 2D flows whereas (3) describes 3D flows and

thus includes a vertical advection term on its left-hand side.

Before presenting numerical results in section 3, it is of interest to note that these experiments will display many of the characteristics of 2D turbulence, in particular the selective decay of enstrophy (e.g., Bretherton and Haidvogel 1976; Mattheaus and Montgomery 1980; Leith 1984). To help understand this point, we first note that two quadratic integral properties associated with (4) and (5) on a periodic domain are the energy and enstrophy relations. The energy equation, obtained by multiplying (4) by $-\psi$ and then integrating over the entire domain, is

$$\frac{d\mathcal{E}}{dt} = \mathcal{G} - 2\mu\mathcal{E} - 2\nu\mathcal{Z}, \quad (6)$$

where $\mathcal{E} = \iint 1/2 \nabla\psi \cdot \nabla\psi \, dx \, dy$ is the energy, $\mathcal{G} = -\iint \psi(f + \zeta) [1 - (f + \zeta)/(f + \zeta_m)] C(x, y) \, dx \, dy$ is the energy generation, and $\mathcal{Z} = \iint 1/2 \zeta^2 \, dx \, dy$ is the enstrophy. Similarly, the enstrophy equation, obtained by multiplying (4) by ζ and then integrating over the full domain, is

$$\frac{d\mathcal{Z}}{dt} = \mathcal{H} - 2\mu\mathcal{Z} - 2\nu\mathcal{P}, \quad (7)$$

where $\mathcal{H} = \iint \zeta(f + \zeta) [1 - (f + \zeta)/(f + \zeta_m)] C(x, y) \, dx \, dy$ is the enstrophy generation and $\mathcal{P} = \iint 1/2 \nabla\zeta \cdot \nabla\zeta \, dx \, dy$ is the palinstrophy (a measure of the overall vorticity gradient). During the advective rearrangement of vorticity, \mathcal{P} can rapidly increase, and for small enough values of ν , \mathcal{P} can surge to values very much larger than its initial value. Thus, \mathcal{P} can provide a useful measure of the formation of prominent asymmetries or mixing events. During the period of large \mathcal{P} , \mathcal{Z} decays rapidly compared to \mathcal{E} , whose rate of decay becomes smaller as \mathcal{Z} becomes smaller. In this way, \mathcal{Z} is selectively decayed over \mathcal{E} .

Because the forced flows evolving from the solution of (4) and (5) can involve complicated vorticity rearrangement processes, it is useful for comparison purposes to derive a hypothetical axisymmetric solution that would occur in the absence of advection and dissipation. We denote this solution by ζ_g , with the subscript g indicating the “generation of vorticity” that would occur with axisymmetric forcing only. Under these conditions, the $\zeta_g(r, t)$ field evolves according to

$$\frac{\partial \zeta_g}{\partial t} = (f + \zeta_g) \left(1 - \frac{f + \zeta_g}{f + \zeta_m} \right) C. \quad (8)$$

With the initial condition $\zeta_g(r, 0) = 0$, (8) has the solution

$$\zeta_g(r, t) = f \left\{ \frac{f + \zeta_m}{f + \zeta_m \exp[-C(r)t]} - 1 \right\}. \quad (9)$$

For $f \ll \zeta_m$ and $C(r)t \ll 1$, (9) can be approximated by $\zeta_g(r, t) \approx f \{ \exp[C(r)t] - 1 \}$, so that initially $\zeta_g(r, t)$ grows exponentially in the region where $C(r) > 0$. At larger times, the growth slows and, in the limit $t \rightarrow \infty$, (9) yields

$$\zeta_g(r, \infty) = \begin{cases} \zeta_m & \text{if } C(r) > 0, \\ 0 & \text{if } C(r) = 0. \end{cases} \quad (10)$$

Hence, in the absence of both advection and dissipation, by restricting nonzero $C(r)$ to an annular region, the vorticity field evolves into an annular ring in which the vorticity has the constant value ζ_m .

It also proves useful for analysis to define an axisymmetric intensity v_{gd} that includes both the generation and dissipation (friction and diffusion) of vorticity but neglects advective processes. The radial vorticity profile associated with v_{gd} , denoted as $\zeta_{gd}(r, t)$, evolves according to

$$\begin{aligned} \frac{\partial \zeta_{gd}}{\partial t} = & (f + \zeta_{gd}) \left(1 - \frac{f + \zeta_{gd}}{f + \zeta_m} \right) C - \mu \zeta_{gd} \\ & + \nu \frac{\partial}{r \partial r} \left(r \frac{\partial \zeta_{gd}}{\partial r} \right). \end{aligned} \quad (11)$$

Solutions to (11) are obtained via numerical integration. The intensity v_{gd} is computed from

$$v_{gd}(r, t) = \frac{1}{r_{\max}} \int_0^{r_{\max}} \zeta_{gd}(\hat{r}, t) \hat{r} d\hat{r}, \quad (12)$$

where r_{\max} is the radius of maximum winds. Comparing $\zeta_{gd}(r, t)$ with $\zeta(x, y, t)$ obtained from (4) provides a way to quantify the contributions of asymmetric motions to a vortex experiencing vorticity generation and dissipation. It should be noted that although the forcing used in (4) parameterizes aspects of a hurricane’s transverse circulation, the 2D barotropic framework does not provide a way to clarify the dynamics of the transverse circulation. Thus, it is not our goal to address the assumptions that are needed in the axisymmetric framework, such as the parameterization of radial mixing/diffusion of angular momentum (Emanuel 1989, 1997), for a hurricane to spin up and attain its potential intensity (Emanuel 1986, 1988, 1995). However, our modeling framework provides an experimental framework for understanding the modification and temporal evolution of barotropic instability and 2D asymmetric flows by idealized diabatic forcing and dissipation.

TABLE 1. Forcing parameters for the four control experiments.

Experiment	r_1 (km)	r_2 (km)	r_3 (km)	r_4 (km)	C_{ew}^{-1} (hr)	ζ_m ($10^{-3} s^{-1}$)
A	20	24	36	40	10.7	4.17
B	24	28	36	40	8.5	4.88
C	28	32	36	40	6.0	6.13
D	32	36	36	40	3.2	8.68

3. Results of the numerical experiments

a. Experimental setup

The numerical methods used to solve (4) and (5) are the same as those described in Schubert et al. (1999). The numerical model uses the Fourier pseudospectral method and fourth-order Runge–Kutta time differencing with $\Delta t = 10$ s. The $200 \text{ km} \times 200 \text{ km}$ doubly periodic domain uses 512×512 collocation points, so that the effective resolution, after dealiasing, is 1.18 km. The coefficient for diffusion is $\nu = 32 \text{ m}^2 \text{ s}^{-1}$. Assuming a vorticity half-life τ_{half} (e.g., Montgomery et al. 2001) of 48 h yields a coefficient of Rayleigh friction $\mu = (\ln 2)/\tau_{\text{half}} \approx 4.01 \times 10^{-6} \text{ s}^{-1}$. The initial condition is a state of rest and $C(r)$ is assumed to take the form of an axisymmetric ring defined by

$$C(r) = C_{ew} \begin{cases} 0, & 0 \leq r \leq r_1, \\ S[(r_2 - r)/(r_2 - r_1)], & r_1 \leq r \leq r_2, \\ 1, & r_2 \leq r \leq r_3, \\ S[(r - r_3)/(r_4 - r_3)], & r_3 \leq r \leq r_4, \\ 0, & r_4 \leq r < \infty, \end{cases} \quad \text{or} \quad (13)$$

where $r = (x^2 + y^2)^{1/2}$ is the radius; $r_1, r_2, r_3,$ and r_4 are specified radii; $S(s) = 1 - 3s^2 + 2s^3$ is the basic cubic Hermite shape function; and C_{ew} is the constant eyewall value of $C(r)$. The values of r_3 and r_4 are the same for all experiments, as listed in Table 1. The values of r_1 and r_2 vary between experiments, with the four choices $r_1 = 20, 24, 28, 32 \text{ km}$ and $r_2 = r_1 + 4 \text{ km}$. The particular selection of geometric parameters used here provides a range of eyewall sizes that compare reasonably with observations (e.g., Jorgensen 1984). The variation in eyewall width allows for an exploration of how barotropic instability varies as vorticity generation becomes confined into a thinner annular region. After carrying out a few further sensitivity tests with different eyewall geometry, we concluded that the four ring widths chosen here capture the essence of how forcing modifies the barotropic instability problem in our modeling framework. Each experiment has the same area-averaged value of $C(r)$ inside $r = 50 \text{ km}$, denoted C_{av} .

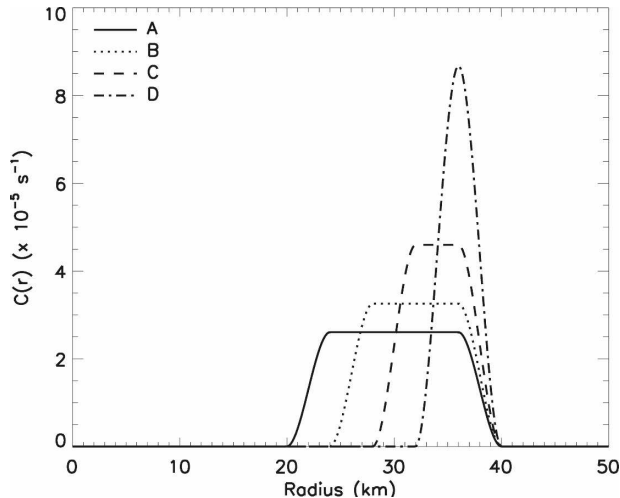


FIG. 1. Plot of $C(r)$ for experiments A–D, in which $r_1 = 20, 24, 28, 32 \text{ km}$, $r_2 = r_1 + 4 \text{ km}$, $r_3 = 36 \text{ km}$, and $r_4 = 40 \text{ km}$.

Later on, we investigate the sensitivity of forced vorticity rings to this parameter. Meanwhile, we fix $C_{av} = 1.0 \times 10^{-5} \text{ s}^{-1}$. Using (13) in this constraint, we obtain

$$C_{ew} = \left[\frac{10(50 \text{ km})^2}{(3r_3^2 + 4r_3r_4 + 3r_4^2) - (3r_1^2 + 4r_1r_2 + 3r_2^2)} \right] C_{av}, \quad (14)$$

from which C_{ew} is computed once the radii $r_1, r_2, r_3,$ and r_4 have been specified. Plots of $C(r)$ for the four experiments are shown in Fig. 1. Corresponding values of the initial e -folding time C_{ew}^{-1} for ζ_g are listed in the sixth column of Table 1.

Concerning the choice of ζ_m , we have required that all experiments yield a $\zeta_g(r, \infty)$ field resulting in a 50 m s^{-1} tangential wind at $r = 50 \text{ km}$. This requires that $(r_4^2 - r_1^2) \zeta_m = (50 \text{ km})^2 (2.0 \times 10^{-3} \text{ s}^{-1})$, which results in the values of ζ_m listed in the last column of Table 1. Figure 2 contains both $\zeta_g(r, t)$ and $\zeta_{gd}(r, t)$ in the region $r_2 < r < r_3$ for experiments A–D. It is clear that dissipation reduces the maximum vorticity achieved and, further, that all curves are logistically limited.

According to (10), the forcing (13) will tend to produce vorticity of magnitude ζ_m in the annular region $r_1 < r < r_4$. The annular rings produced in experiments A–D are characterized by $r_1/r_4 = 0.5, 0.6, 0.7,$ and 0.8 , respectively. According to the linear stability theory of unforced vorticity rings (see Fig. 2 of Schubert et al. 1999), the growth rate of instability (i.e., ν_i), normalized by the average vorticity within the vortex, depends strictly on geometry because of the restriction that all nonzero relative vorticity is located within the annular region of forcing. Cases A–D are expected to become

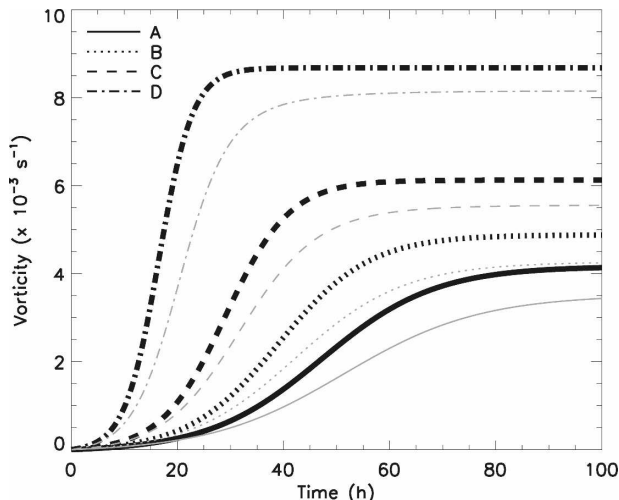


FIG. 2. Time evolution of $\zeta_g(r, t)$ (thick black line) and $\zeta_{gd}(r, t)$ (thin gray line) in the region $r_2 < r < r_3$ for the control experiments A–D.

unstable to azimuthal wavenumbers 3–5 for the limiting case given in (10), with the fastest growth rate and highest wavenumber occurring for the thinnest ring. However, despite some broadening of the vorticity profile by diffusion, the Hermite polynomial transitions still effectively narrow the width of the annular vorticity region at finite times. Hence, the simulated instability is expected to take place at higher wavenumbers than suggested in (10).

b. Results

We recall that experiments A–D are spun up from a state of rest. To facilitate barotropic instability in the developing vorticity ring, random vorticity perturbations containing an amplitude of 0.5% of the relative vorticity are added 12 h into the simulation within the interval $20 \text{ km} \leq r \leq 40 \text{ km}$. This time marks a period when the incipient vortex ring is building at nearly an exponential rate. Sensitivity tests show that the timing at which these small-amplitude, random perturbations are added to the flow do in fact change the details of evolution in each experiment in accordance with the nonlinear nature of the model. However, the evolution of vortex intensity is less sensitive to the nature of the weak impulsive forcing.

As an example of the type of evolution that can transpire in the situation of forced vorticity rings, Fig. 3 provides snapshots of the vorticity field in experiment C over 10 days of simulation. Within the first day, vorticity builds into a ring structure. By 1.3 days, six mesovortices have formed even though the vorticity within the ring is far from achieving its logistic upper bound.

The initial development of six mesovortices in the simulation indicates that the most unstable growth rate is found in wavenumber 6. Indeed, applying the eigensolver described in appendix B of Reasor et al. (2000) to the corresponding ζ_{gd} profile at 1.3 h, barotropic instability is expected to occur with maximum growth rates found in wavenumbers 5 and 6. This result contrasts with the wavenumber-3 instability predicted using the three-region distribution of ζ_g suggested in (10), which does not account for diffusion, dissipation, the smooth transition of vorticity at the edges of the annular ring, or the zero circulation constraint providing a negative vorticity almost an order of magnitude smaller than the Coriolis force outside the annulus of enhanced vorticity. After mesovortex formation, vorticity within these mesovortices continues to intensify over the following day because they overlap the annular region of vorticity generation. By 1.9 days, vortex merger events have reduced the number of mesovortices to four. Between 1.9 and 2.5 days, a vigorous inward-directed vorticity mixing event takes place and a monopole of vorticity temporarily forms. Except for the vorticity generation within both the vortex ring and resulting mesovortices, this particular evolution resembles the unforced vorticity mixing events portrayed in Schubert et al. (1999). After 3 days, experiment C deviates markedly from the results in Schubert et al. (1999). As forcing and axisymmetrization act within the vortex, vorticity continues to organize and regenerate into an annulus roughly coincident with the region of vorticity generation. Although no distinct monopole forms after the initial mixing event, numerous wavenumber-2 through wavenumber-4 asymmetries repeatedly form and axisymmetrize within the annulus of enhanced vorticity. After approximately 7 days, the maximum wind speed eventually stops increasing because of logistic constraints.

Figure 4a contains the radial profiles of ζ_{gd} and the azimuthal average of the ζ field shown in the lower right-hand panel of Fig. 3 (i.e., experiment C at 10 days). As a result of continuous forcing, the radial profile of vorticity from the model output is still peaked in the vicinity of vorticity generation, but the radial profile is broader than the corresponding ζ_{gd} profile because of episodic vorticity mixing events. Although according to eigensolver computations (Reasor et al. 2000) the simulated vortex at 10 days is slightly unstable at wavenumber 2 with an e -folding growth time of 196.1 min (Table 2), the corresponding ζ_{gd} profile contains an e -folding growth time of 24.8 min at wavenumber 4. Thus, episodic vorticity mixing events resulting from the persistence of barotropic instability in the presence of continuous forcing have brought the vortex closer to a

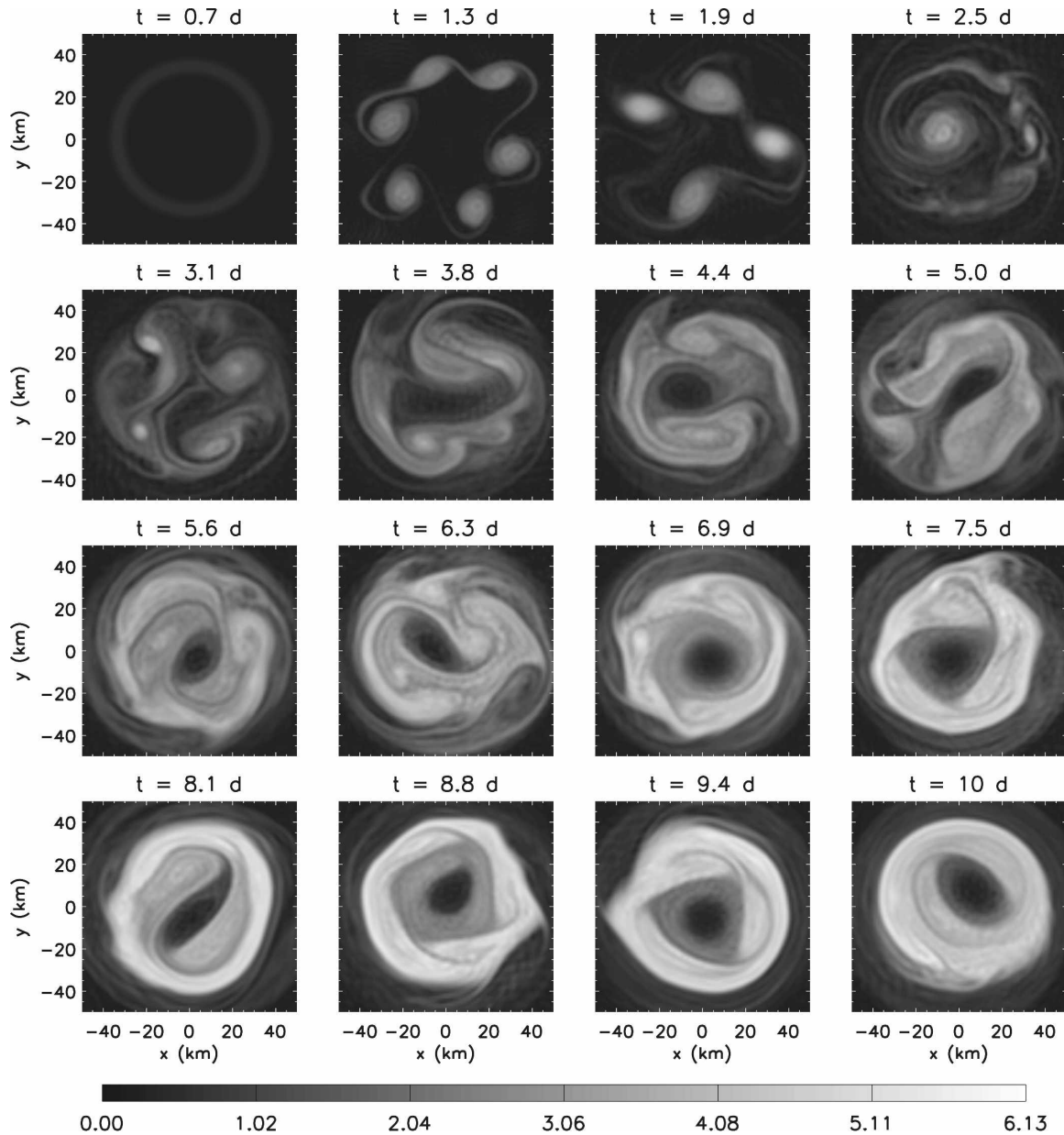


FIG. 3. Time evolution (days) of vorticity ($\times 10^{-3} \text{ s}^{-1}$) in experiment C.

barotropically neutral state. As a note of interest, the azimuthal-average vorticity in the simulation shares more similarities than the corresponding ζ_{gd} profile with radial vorticity profiles obtained from flight-level wind data in mature hurricanes (e.g., Kossin and Eastin 2001; Mallen et al. 2005). Mature hurricanes often contain an annulus of enhanced vorticity near the eyewall but still have enhanced vorticity within the eye. Furthermore, both observations and the azimuthal-average vorticity profile derived from experiment C contain a skirt of enhanced vorticity immediately outside of the

radius of maximum winds. The broadened vorticity profile in the simulation results from substantial events of asymmetric vorticity advection. Figure 4b contains the tangential wind profiles corresponding to the vorticity profiles in Fig. 4. As a result of episodic vorticity mixing events, wind speeds in the 2D simulation exceed their v_{gd} and winds spin up at radii inside the ring of vorticity generation.

The vorticity evolution documented in the above example shares a number of similarities with the vorticity evolution in the other experiments. Consistent with the

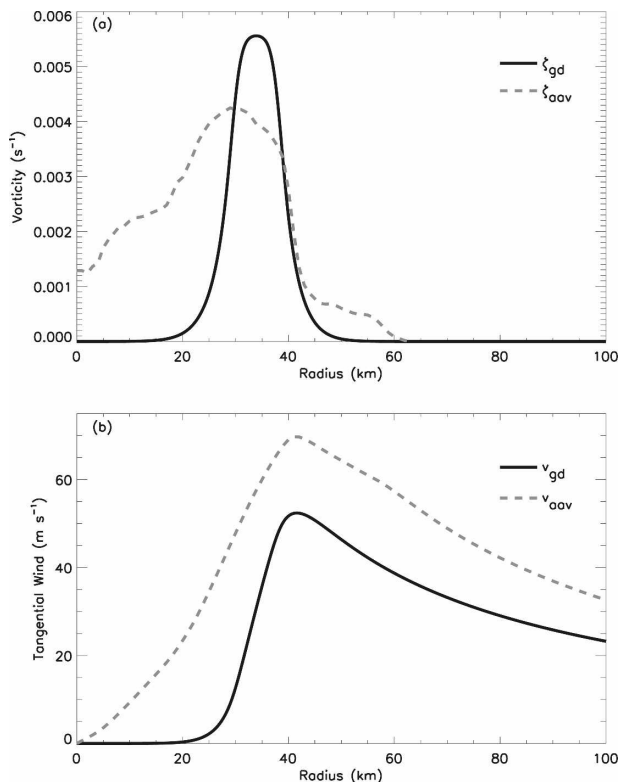


FIG. 4. (a) Radial profiles of ζ_{gd} (black curve) and the azimuthal-average simulated vorticity ζ_{aav} (gray curve) in experiment C after 10 days of simulation; (b) radial profiles of tangential wind corresponding to each vorticity profile.

linear theory of barotropic instability, the progressively thinner rings of experiments A, B, C, and D initially collapse into 3, 4, 6, and 9 mesovortices, respectively. Moreover, mesovortices form more rapidly in the situation of thinner rings and enhanced $C(r)$. After initial mesovortices appear, each experiment contains a subsequent series of mixing events or periods of marked asymmetric vorticity patterns. With the exception of the thickest ring (experiment A), each experiment contains an initial collapse of mesovortices into a central monopole, followed by reorganization of enhanced vorticity into a ring. Although mesovortices form earliest for the thinnest ring (experiment D), monopole forma-

TABLE 2. The most unstable wavenumber (n) and the associated e -folding time associated with the growth rate (ν_i) for the radial profiles of azimuthal-average $\zeta(x, y)$ and $\zeta_{gd}(r)$ at 10 days.

Experiment	n_{sim}	$\nu_{i,sim}^{-1}$ (min)	n_{gd}	$\nu_{i,gd}^{-1}$ (min)
A	2	490.2	3	71.2
B	2	877.2	3	41.5
C	2	196.1	4	24.8
D	2	463.0	5	14.4

tion is delayed for roughly 3 days because mesovortices persist predominantly in a wavenumber-5 mesovortex pattern resembling vortex crystals (e.g., Kossin and Schubert 2001). The number of distinct monopole formations achieved in experiments B, C, and D is 3, 1, and 2, respectively, although the amplitude and frequency of asymmetric patterns appear to increase with decreasing ring width and increasing $C(r)$.

The properties of forced vorticity rings are further highlighted in Fig. 5. We recall that periods of enhanced palinstrophy \mathcal{P} denote significant asymmetries or mixing episodes because enstrophy is rapidly transferred to high wavenumbers during such events. As depicted in Fig. 5a, numerous enhanced \mathcal{P} events occur for all PV rings. Experiment D (i.e., the thinnest and most intense ring) experiences an enhanced \mathcal{P} event less than 1 day into the simulation, followed by experiment C at about 1.3 days, experiment B at about 1.7 days, and experiment A around 2.5 days. As illustrated in experiment C (Fig. 3), these initial spikes in palinstrophy are associated with the formation of mesovortices. In experiment D, a substantial secondary spike in \mathcal{P} appears between 3.5 and 4 days, indicating the collapse of mesovortices into an interior monopole of vorticity. Weaker-amplitude mesovortices in experiments A–C form and subsequently merge and axisymmetrize more rapidly than in experiment D, so secondary spikes in palinstrophy are not as pronounced. After an initial vortex ring breakdown, occasional spikes in \mathcal{P} appear later on in all simulations, indicating the episodic nature of strong asymmetric formations and mixing events. The palinstrophy curves indicate that thinner vorticity rings containing elevated $C(r)$ experience more vigorous periods of asymmetric flow and vorticity mixing, confirming the visual characteristics described above.

Figure 5b shows the time evolution of both the maximum tangential winds achieved in the simulation and the corresponding v_{gd} for experiments A–D. The salient point of Fig. 5b is that asymmetric vorticity mixing resulting from barotropic instability yields dramatic differences in the maximum tangential winds found in the simulations and the corresponding values of v_{gd} . For experiments A–D, an initial barotropic instability event slows the rate of intensification because vorticity generation becomes geometrically less efficient. In other words, the fractional coverage of enhanced vorticity within the annular region of convergence is diminished when vorticity concentrates into compact mesovortices. Inward radial mixing eventually follows the formation of mesovortices in each experiment. These inward mixing events are associated with the secondary spikes in the palinstrophy curves provided in Fig. 5a. In experiments C and D, weakening actually occurs during this

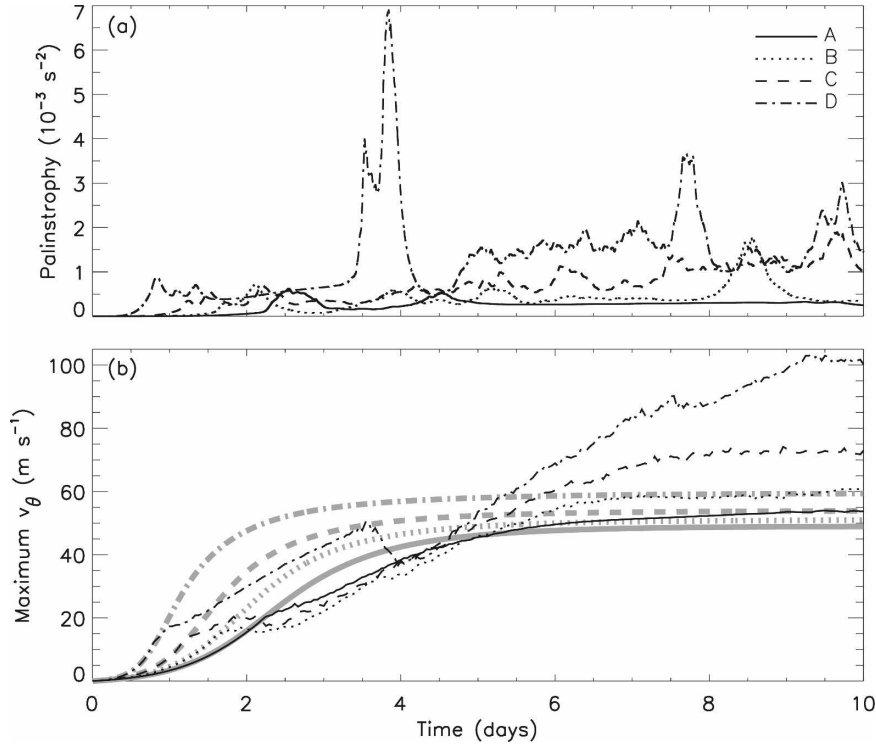


FIG. 5. The time evolution of (a) palinstrophy and (b) simulated maximum tangential wind (m s^{-1} ; thin black line) and v_{gd} (m s^{-1} ; thick gray line) for experiments A–D.

stage. However, the intensities of all vortices eventually exceed v_{gd} with subsequent asymmetric activity. The departure from a storm's v_{gd} is enhanced for the thinner and more intense forcing. More frequent mixing and asymmetric activity bring higher vorticity into the center of the vortex; thus, the circulation exceeds that predicted in (11) for the axisymmetric evolution.

As seen in Fig. 5b, each experiment achieves a nearly steady intensity by around 10 days. At 10 days, eigen-solver calculations summarized in Table 2 confirm that the azimuthal-average ζ profiles possess growth rates roughly 1–2 orders of magnitude smaller than their corresponding ζ_{gd} profiles. The azimuthal-average ζ profile for each experiment is most unstable at wavenumber 2, which is smaller than the wavenumbers associated with the most unstable growth rates in the corresponding ζ_{gd} profiles. Thus, in the presence of continued forcing, asymmetric motions resulting from barotropic instability seem to ultimately lead to broadened vortices that are more barotropically neutral.

4. The sensitivity of forced vorticity rings to changes in vorticity convergence and Rayleigh friction

The values chosen above for the average convergence C_{av} and for the Rayleigh friction coefficient μ are

somewhat arbitrary. It is therefore worthwhile to explore the sensitivity of forced vorticity rings to different magnitudes of C_{av} and μ . Twenty-five experiments are performed for the ring geometry defined in experiment D (i.e., $r_1 = 32 \text{ km}$ and $r_2 = 36 \text{ km}$). The area-average convergence C_{av} is set to 2, 4, 6, 8, and $10 \times 10^{-6} \text{ s}^{-1}$. The Rayleigh friction coefficient is allowed to vary over the range of $\tau_{half} = 24, 36, 48, 60,$ and 72 h . To speed up the rate at which initial instabilities form, the initial condition now consists of a vorticity monopole of tropical storm strength, as depicted in Fig. 6. Within $r \leq r_3$, the initial vorticity is fixed at $1.25 \times 10^{-3} \text{ s}^{-1}$. The basic cubic Hermite shape function is used to smooth vorticity off to zero within the interval $r_3 \leq r \leq r_4$. To initiate barotropic instabilities in the numerical simulations, randomly distributed vorticity perturbations containing amplitudes of 0.5% of the initial vorticity are added to our initial condition. The initial vortex contains a maximum tangential wind of about 23 m s^{-1} at $r = 38.9 \text{ km}$.

First, we isolate the role of convergence in our simulations by keeping the Rayleigh friction coefficient fixed at $\tau_{half} = 48 \text{ h}$ and varying convergence. According to the expression for ζ_g given in (9), the limiting solution as $t \rightarrow \infty$ given in (10) implies that the final axisymmetric vortex is insensitive to the rate of convergence. However, ζ_{gd} varies with the rate of convergence

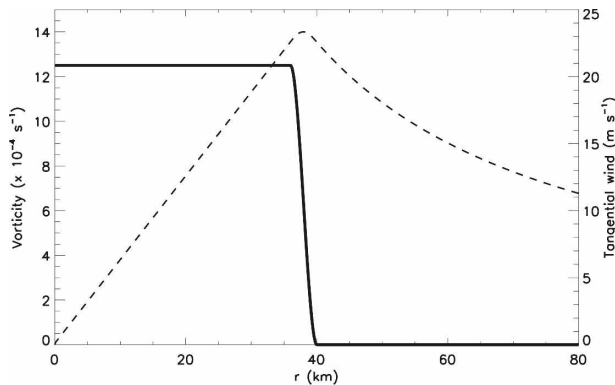


FIG. 6. The initial vorticity ($\times 10^{-4} \text{ s}^{-1}$; solid line) and tangential wind (m s^{-1} ; dashed line) profiles in the sensitivity experiments.

for a fixed time scale of friction because frictional dissipation is proportional to the magnitude of vorticity. Thus, a sensitivity of vorticity rings to vorticity convergence is anticipated in the presence of dissipation. We are interested in further understanding the impact of varying convergence in the presence of asymmetric motions.

In Schubert et al. (1999), a dimensionless growth rate of instability ν_i/ζ_{av} was used to quantify barotropic instability for different three-region vorticity rings in the linearized nondivergent barotropic model, where ν_i is the imaginary (unstable) part of the complex eigenvalues associated with counterpropagating vortex Rossby waves and ζ_{av} is the average vorticity within the region $0 \leq r \leq r_4$. Figure 7a shows the maximum dimensionless growth rate associated with each increment of average convergence C_{av} . These growth rates are computed from a three-region approximation of ζ_{gd} and therefore are only relevant to our simulations before the initial mixing event. However, the dimensionless growth rates conceptually show how the initial instability varies with changing C_{av} . Whereas vorticity is generated within a ring, Rayleigh friction acts on vorticity in the center of the vortex. Thus, ν_i/ζ_{av} rapidly grows as vorticity generation takes place and unstable conditions form much more quickly in the situation of stronger convergence. Also, in contrast with experiments A–D, the instabilities predicted by the linear theory shift to smaller wavenumbers in time.

As the palinstrophy curves in Fig. 7b demonstrate, the simulated timing of an initial episode of barotropic instability behaves nearly in accordance with the linear theory. For $C_{\text{av}} = 10 \times 10^{-6} \text{ s}^{-1}$, an initial instability event occurs by 12 h into the simulation, which is about 30 h earlier than in the experiment with $C_{\text{av}} = 2 \times 10^{-6} \text{ s}^{-1}$. Regardless, the initial vortex ring collapses into 12 mesovortices in each experiment. Also, it is noteworthy

that simulations with stronger convergence continue to produce substantial \mathcal{P} events throughout the simulation, whereas the weakest vorticity generation fails to produce notable mixing events after the vorticity ring initially breaks down into mesovortices.

Figure 7c provides both v_{gd} and the maximum simulated tangential winds associated with each value of convergence. In the simulations, initial instability events are clearly denoted by sharp downward transitions in the maximum tangential wind speed that fall well below their corresponding values of v_{gd} . This result varies slightly from experiments A–D above, in which initial instability events mark a transitional period of longer-lived mesovortices. As a result, those experiments only experienced a lower rate of intensification until complete inward mixing of vorticity led to temporary weakening in the thinner rings. However, in the presence of positive relative vorticity in the eye of these vortices, inward mixing quickly follows mesovortex formation in the sensitivity experiments. Thus, the intensity of these vortices is weakened immediately upon the emergence of barotropic instability. Now, if convergence is sufficiently strong, the maximum tangential wind recovers at a nearly linear rate and eventually exceeds its associated v_{gd} . Comparing Figs. 7b and 7c, a direct relationship between the frequency and magnitude of enhanced \mathcal{P} events and intensification appears to exist—that is, the combination of increased inward vorticity mixing and enhanced vorticity generation results in greater intensification for rings containing $C_{\text{av}} > 4 \times 10^{-6} \text{ s}^{-1}$.

We now briefly explore the impact of Rayleigh friction on the dynamics of forced vortices. Figure 8a shows dimensionless growth rates of barotropic instability computed from a three-region approximation of v_{gd} for $\tau_{\text{half}} = 24, 36, 48, 60,$ and 72 h and $C_{\text{av}} = 10 \times 10^{-6} \text{ s}^{-1}$. Because friction decreases vorticity within the central region enclosed by the ring of vorticity generation, stronger friction contributes to slightly more unstable conditions. However, the onset timing of instability is barely changed by friction, as further illustrated in Fig. 8b. Furthermore, vorticity rings in each experiment initially break down into 12 mesovortices once again. After an initial vorticity mixing event, the intensity of subsequent mixing events is dampened in the presence of stronger friction. Unsurprisingly, the curves of v_{gd} in Fig. 8c show that increased friction decreases the impact of vorticity generation on vortex intensification. The simulations show that the impact of friction on wind speeds is more pronounced when asymmetric motions are permitted.

In the course of carrying out these sensitivity experiments, it was recognized that if friction is sufficiently

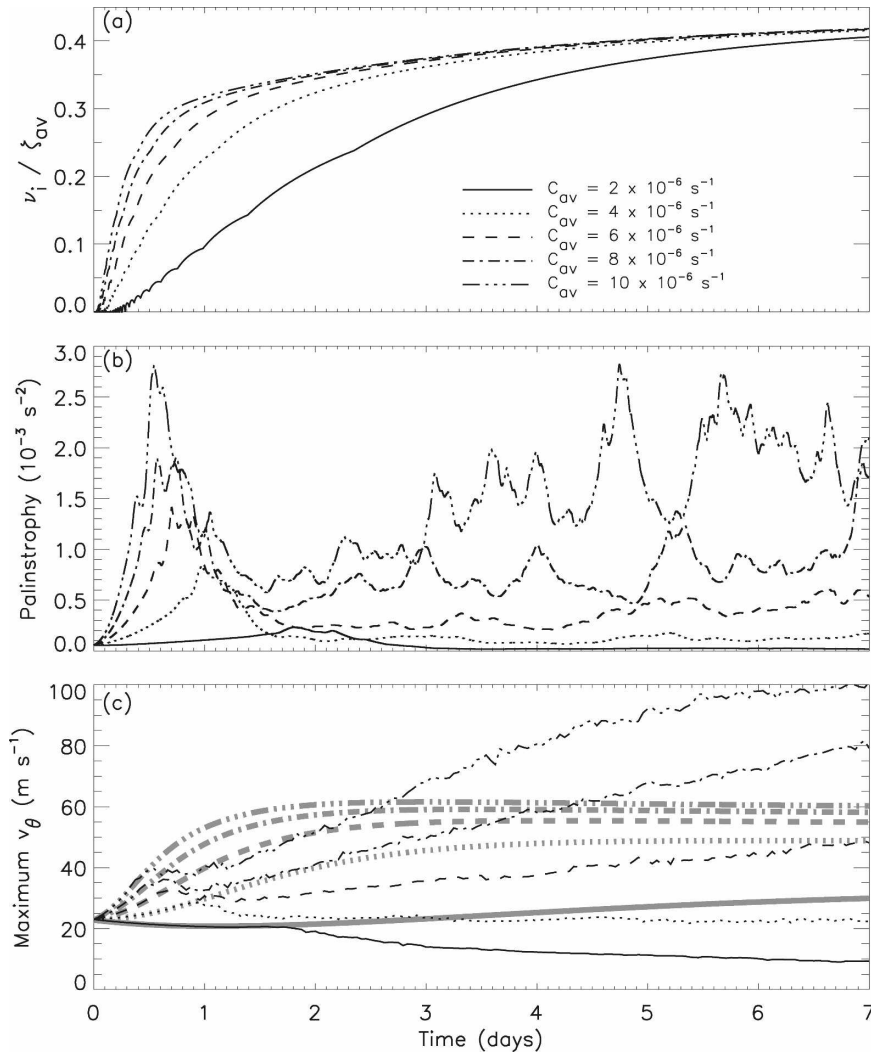


FIG. 7. (a) Dimensionless growth rates of barotropic instability for $r_1 = 32$ km and $r_2 = 36$ km, as computed from the ζ_{gd} corresponding to $\tau_{half} = 48$ h and $C_{av} = 2\text{--}10 \times 10^{-6} \text{ s}^{-1}$, and corresponding (b) palinstrophy and (c) maximum tangential winds in the simulations. For reference, profiles of v_{gd} are plotted in thick gray.

strong or if the vorticity generation is weak enough, a vortex will essentially vanish after an initial barotropic instability event. A clear example of this phenomenon is depicted for the weak convergence situation in Fig. 7c. As another example, Fig. 9a shows the evolution of vorticity subject to strong dissipation and weak convergence, where $\tau_{half} = 24$ h and $C_{av} = 2 \times 10^{-6} \text{ s}^{-1}$. Although this situation may be of academic interest, the weak convergence may be analogous to weak eye-wall convection in a hurricane encountering a marginal thermodynamic environment, such as an eastern Pacific storm that crosses into cooler sea surface temperatures. In this extreme situation, vorticity is dissipated everywhere from the beginning of the simulation. However, in the annular region of vorticity generation, dissipation

of vorticity is slower than in the eye. Hence, high wave-number instabilities form and mesovortex production takes place. These mesovortices merge during the first day, but they continue to rotate near the region of vorticity generation. Nonetheless, these mesovortices continue to weaken even though they continually merge with surrounding vorticity and experience forcing. The vorticity field in the simulation contrasts with its associated ζ_{gd} , where vorticity within the region of vorticity generation reaches $1.7 \times 10^{-3} \text{ s}^{-1}$.

The maximum tangential winds and v_{gd} associated with the experiment shown in Fig. 9a is provided in Fig. 9b. As the vorticity ring breaks down into mesovortices, the maximum tangential winds weaken below v_{gd} . Consistent with the decaying vorticity, the intensity of the

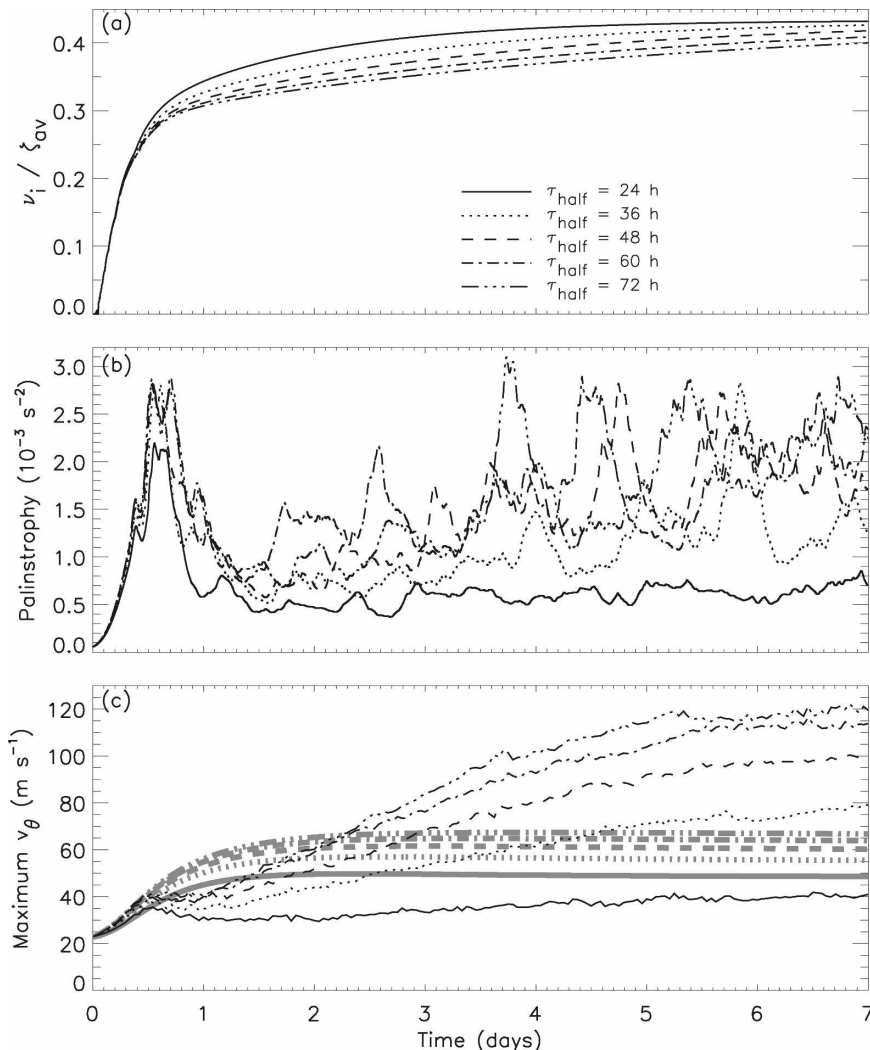


FIG. 8. As in Fig. 7, but for $C_{av} = 10 \times 10^{-6} \text{ s}^{-1}$ and $\tau_{\text{half}} = 24, 36, 48, 60,$ and 72 h .

vortex continues to weaken to a state that would be unrecognizable as a tropical disturbance in real observations. The energy principle (6) helps explain why this vortex disappears. Similar to experiments of unforced 2D turbulence, the diffusion term $-2\nu Z$ is insignificant in terms of the kinetic energy in this simulation. However, it turns out that the dissipation term $-2\mu E$ dominates the energy generation term G , on average, by 233% throughout the simulation, which significantly decreases the kinetic energy. Thus, the vortex weakens under such adverse conditions. Moreover, corresponding closely with the analyzed intensity of the vortex, the magnitude of the energy generation term decreases more rapidly as mesovortices form. Hence, asymmetries further weaken vortices in an unfavorable environment of weak vorticity generation and strong dissipation as vorticity generation becomes more localized

with respect to the juxtaposition of mesovortices and the fixed annular region of convergence.

Figure 9c demonstrates that, if allowed to evolve another 7 days, our dissipating vortex continues to slowly weaken. For reference, the evolution of v_{gd} starting from a state of rest at 7 days is also shown in Fig. 9c. This v_{gd} increases beyond the weakened state of the simulated vortex, suggesting again that asymmetries prevent axisymmetric convergence from rebuilding the vortex. As another experiment, we neglect Rayleigh friction while starting with the initial conditions given by the simulation vorticity field in Fig. 9b at 7 days. Indeed, vorticity in this situation is allowed to build up and the vortex slowly intensifies. However, the corresponding v_{gd} is far greater than the intensity in the simulation, which again demonstrates the negative impact of asymmetries on vorticity generation.

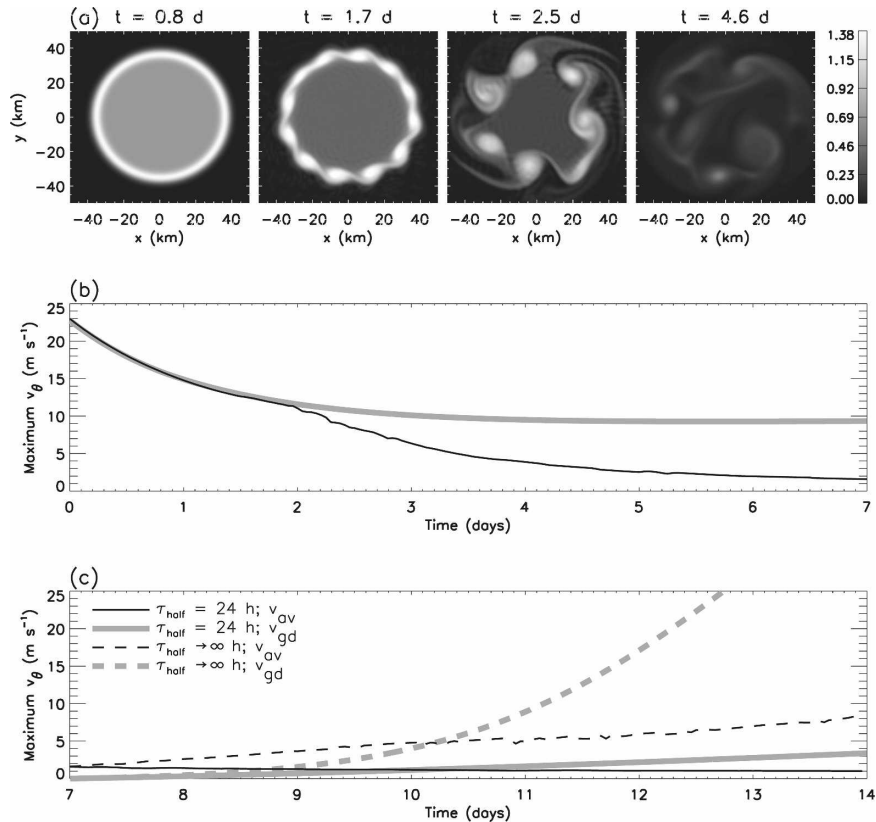


FIG. 9. (a) Time evolution (days) of vorticity ($\times 10^{-3} \text{ s}^{-1}$) in experiment D with $C_{\text{ave}} = 2 \times 10^{-6} \text{ s}^{-1}$ and $\tau_{\text{half}} = 24$ h, (b) the associated evolution of v_{gd} (thick gray) and simulated maximum tangential wind (thin black; m s^{-1}), and (c) continued evolution of the simulated maximum tangential wind maintaining $\tau_{\text{half}} = 24$ h (thin black) and allowing $\tau_{\text{half}} \rightarrow \infty$ (thin dashed), along with their corresponding v_{gd} initialized at a resting state at 7 days (gray solid and dashed).

5. Conclusions

In summary, we have used a forced, 2D barotropic model to study the impact of diabatic and frictional effects on barotropic instability and associated intensity changes. The idealized model used here is a drastic simplification of the intricate moist dynamics occurring in real hurricanes. Inspired by the behavior of PV in eyewalls resolved in full-physics, high-resolution hurricane simulations, our diabatic heating is parameterized in the vorticity equation using a logistically limited analog of the divergence term. This vorticity generation is assumed to take place in an annular region representative of an eyewall. Neglecting major rainbands and outer eyewalls, this is a reasonable approximation to a mature hurricane for our purposes, but such an assumption obviously limits the applicability of these results in the context of real hurricanes because eyewalls constantly change size during the course of a hurricane life cycle in response to various environmental and internal

dynamical factors. As another note of caution, incipient hurricanes are often fundamentally asymmetric and lack an eye, so the geometry of our forcing may restrict our results to mature hurricanes.

With the strict assumptions of this paper in mind, our results support some of the primary conclusions found in the literature of barotropic instability associated with unforced PV rings. Similar to the previous studies, the forced nondivergent barotropic model suggests that instabilities more readily develop for thinner and more intense vorticity rings. A vortex ring's transition into mesovortices and the subsequent inward vorticity mixing slows intensification or even weakens a vortex so that the vortex's intensity falls below the intensity it would achieve if asymmetric motions were not permitted. In contrast with the unforced experiments, sufficiently strong vorticity generation allows vorticity to eventually rebuild into an annular ring surrounding the core of mixed vorticity. Rayleigh friction continually dissipates vorticity, further supporting subsequent un-

stable rings of vorticity because the eye vorticity decreases relative to the ring of vorticity generation. Thus, episodic mixing events can continue to unfold as an elevated annulus of vorticity is continually regenerated. For an ideal combination of dissipation and vorticity generation, a vortex can eventually intensify beyond its axisymmetric intensity achieved by forcing alone because asymmetric mixing contributes to an enhanced radial profile of vorticity. After sufficiently many vorticity mixing events, the forced vortex tends toward a more barotropically stable state than a corresponding forced vortex that does not experience asymmetric flow. The above properties of forced vorticity rings apply to a variety of ring widths, which suggests that the principles of this study may still apply to hurricanes with temporal variations in eyewall width and diameter.

Although further examination of these idealized concepts in the analysis of real hurricane observational data may prove illuminating, existing observational studies lend some support to the occurrence of the transient brake mechanism and episodic mixing. For example, Eastin et al. (2006) and Reasor et al. (2009) documented vorticity mixing events during the rapid intensification of Hurricane Guillermo (1997). Kossin and Eastin (2001) also observed significant mixing events in hurricane observational data, but they most often found mixing to take place at maximum intensity. This latter observational study is also interesting in light of our experiment containing strong dissipation and weak vorticity generation. In this experiment, the initial vortex effectively vanishes as mesovortex formation makes vorticity generation even less efficient in the maintenance of the vortex. Thus, it may be of interest to understand whether real hurricanes become increasingly susceptible to marginal environments (e.g., cooler sea surface temperatures) during barotropic instability events.

As we have seen, the forced barotropic model can produce mixing events in which the high vorticity in the eyewall is transported radially into the eye. The generalization to a stratified fluid involves the radial transport of PV. In the high-resolution hurricane simulation of Yau et al. (2004), PV mixing appears to be confined mostly to the lower levels where the PV ring has a smaller diameter than it has at upper levels. If PV is transported radially inward at low levels, it should result, via the PV invertibility principle, in both increased vorticity and increased static stability in the lower levels of the eye. Hurricanes are known to have high static stability and even temperature inversions at lower levels in the eye. Such thermal structures have often been interpreted as primarily due to thermal processes associated with eye subsidence and boundary layer turbu-

lence, by analogy with the trade wind inversion that occurs just above fair weather cumulus. However, the above PV mixing argument suggests that dynamical processes can also play a role in the development of enhanced low-level static stability in the hurricane eye. On the other hand, the 3D hurricane simulation described in Yang et al. (2007) contained the most significant PV mixing at mid to upper levels in the eye, which led to an elevated PV bridge structure. Thus, continued examination of PV mixing in high-resolution model simulations of hurricanes may clarify the various pathways by which barotropic instability is realized in a variety of situations of realistic diabatic heating in 3D vortices.

Acknowledgments. We thank Mark DeMaria, Brian McNoldy, Richard Taft, and Jonathan Vigh for their comments. The eigensolver used to assess the stability of smooth vorticity profiles was provided by Michael Montgomery. Advice and commentary from Matthew Eastin and an anonymous reviewer greatly improved the clarity of this manuscript. This research was supported by NSF Grants ATM-0435694 and ATM-0435644.

REFERENCES

- Bell, M. M., and M. T. Montgomery, 2008: Observed structure, evolution, and potential intensity of Category 5 Hurricane Isabel (2003) from 12 to 14 September. *Mon. Wea. Rev.*, **136**, 2023–2046.
- Bretherton, F., and D. Haidvogel, 1976: Two-dimensional turbulence above topography. *J. Fluid Mech.*, **78**, 129–154.
- Cram, T. A., J. Persing, M. T. Montgomery, and S. A. Braun, 2007: A Lagrangian trajectory view on transport and mixing processes between the eye, eyewall, and environment using a high-resolution simulation of Hurricane Bonnie (1998). *J. Atmos. Sci.*, **64**, 1835–1856.
- DeMaria, M., and J. Kaplan, 1994: A statistical hurricane intensity prediction scheme (SHIPS) for the Atlantic Basin. *Wea. Forecasting*, **9**, 209–220.
- Dunion, J. P., and C. S. Velden, 2004: The impact of the Saharan air layer on Atlantic tropical cyclone activity. *Bull. Amer. Meteor. Soc.*, **85**, 353–365.
- Dvorak, V. F., 1984: Tropical cyclone intensity analysis using satellite data. NOAA Tech. Rep. NESDIS 11, Washington, DC, 47 pp. [Available from National Technical Information Service, 5285 Port Royal Rd., Springfield, VA 22161.]
- Eastin, M. D., P. D. Reasor, D. S. Nolan, F. D. Marks Jr., and J. F. Gamache, 2006: The evolution of low-wavenumber vorticity during rapid intensification: A dual-Doppler analysis. Preprints, *27th Conf. on Hurricanes and Tropical Meteorology*, Monterey, CA, Amer. Meteor. Soc., 4B.6.
- Emanuel, K. A., 1986: An air–sea interaction theory for tropical cyclones. I: Steady-state maintenance. *J. Atmos. Sci.*, **43**, 585–604.
- , 1988: The maximum intensity of hurricanes. *J. Atmos. Sci.*, **45**, 1143–1155.

- , 1989: The finite-amplitude nature of tropical cyclogenesis. *J. Atmos. Sci.*, **46**, 3431–3456.
- , 1995: Sensitivity of tropical cyclones to surface exchange coefficients and a revised steady-state model incorporating eye dynamics. *J. Atmos. Sci.*, **52**, 3969–3976.
- , 1997: Some aspects of hurricane inner-core dynamics and energetics. *J. Atmos. Sci.*, **54**, 1014–1026.
- , 2000: A statistical analysis of tropical cyclone intensity. *Mon. Wea. Rev.*, **128**, 1139–1152.
- , C. DesAutels, C. Holloway, and R. Korty, 2004: Environmental control of tropical cyclone intensity. *J. Atmos. Sci.*, **61**, 843–858.
- Gray, W. M., 1968: Global view of the origin of tropical disturbances and storms. *Mon. Wea. Rev.*, **96**, 669–700.
- Hausman, S. A., K. V. Ooyama, and W. H. Schubert, 2006: Potential vorticity structure of simulated hurricanes. *J. Atmos. Sci.*, **63**, 87–108.
- Jorgensen, D., 1984: Mesoscale and convective-scale characteristics of mature hurricanes. Part II: Inner core structure of Hurricane Allen (1980). *J. Atmos. Sci.*, **41**, 1287–1311.
- Knaff, J. A., J. P. Kossin, and M. DeMaria, 2003: Annular hurricanes. *Wea. Forecasting*, **18**, 204–223.
- Kossin, J. P., and M. D. Eastin, 2001: Two distinct regimes in the kinematic and thermodynamic structure of the hurricane eye and eyewall. *J. Atmos. Sci.*, **58**, 1079–1090.
- , and W. H. Schubert, 2001: Mesovortices, polygonal flow patterns, and rapid pressure falls in hurricane-like vortices. *J. Atmos. Sci.*, **58**, 2196–2209.
- , and —, 2004: Mesovortices in Hurricane Isabel. *Bull. Amer. Meteor. Soc.*, **85**, 151–153.
- , —, and M. T. Montgomery, 2000: Unstable interactions between a hurricane's primary eyewall and a secondary ring of enhanced vorticity. *J. Atmos. Sci.*, **57**, 3893–3917.
- , B. D. McNoldy, and W. H. Schubert, 2002: Vortical swirls in hurricane eye clouds. *Mon. Wea. Rev.*, **130**, 3144–3149.
- Kwon, Y. C., and W. M. Frank, 2005: Dynamic instabilities of simulated hurricane-like vortices and their impacts on the core structure of hurricanes. Part I: Dry experiments. *J. Atmos. Sci.*, **62**, 3955–3973.
- Leith, C. E., 1984: Minimum enstrophy vortices. *Phys. Fluids*, **27**, 1388–1395.
- Mallen, K. J., M. T. Montgomery, and B. Wang, 2005: Reexamining the near-core radial structure of the tropical cyclone circulation: Implications for vortex resiliency. *J. Atmos. Sci.*, **62**, 408–425.
- Mashiko, W., 2005: Polygonal eyewall and mesovortices structure in a numerically simulated Typhoon Rusa. *SOLA*, **1**, 29–32.
- Matthaeus, W. H., and D. Montgomery, 1980: Selective decay hypothesis at high mechanical and magnetic Reynolds numbers. *Ann. N. Y. Acad. Sci.*, **357**, 203–222.
- Merrill, R. T., 1988: Environmental influences on hurricane intensification. *J. Atmos. Sci.*, **45**, 1678–1687.
- Montgomery, M. T., H. D. Snell, and Z. Yang, 2001: Axisymmetric spindown dynamics of hurricane-like vortices. *J. Atmos. Sci.*, **58**, 421–435.
- , V. A. Vladimirov, and P. V. Denissenko, 2002: An experimental study on hurricane mesovortices. *J. Fluid Mech.*, **471**, 1–32.
- Muramatsu, T., 1986: Trochoidal motion of the eye of Typhoon 8019. *J. Meteor. Soc. Japan*, **64**, 259–272.
- Nolan, D. S., and M. T. Montgomery, 2000: The algebraic growth of wavenumber-1 disturbances in hurricane-like vortices. *J. Atmos. Sci.*, **57**, 3514–3538.
- , and —, 2002: Nonhydrostatic, three-dimensional perturbations to balanced, hurricane-like vortices. Part I: Linearized formulation, stability, and evolution. *J. Atmos. Sci.*, **59**, 2989–3020.
- , and L. D. Grasso, 2003: Nonhydrostatic, three-dimensional perturbations to balanced, hurricane-like vortices. Part II: Symmetric response and nonlinear simulations. *J. Atmos. Sci.*, **60**, 2717–2745.
- , M. T. Montgomery, and L. D. Grasso, 2001: The wavenumber-1 instability and trochoidal motion of hurricane-like vortices. *J. Atmos. Sci.*, **58**, 3243–3270.
- Ooyama, K. V., 1990: A thermodynamic foundation for modeling the moist atmosphere. *J. Atmos. Sci.*, **47**, 2580–2593.
- , 2001: A dynamic and thermodynamic foundation for modeling the moist atmosphere with parameterized microphysics. *J. Atmos. Sci.*, **58**, 2073–2102.
- Persing, J., and M. T. Montgomery, 2003: Hurricane superintensity. *J. Atmos. Sci.*, **60**, 2349–2371.
- Reasor, P. D., M. T. Montgomery, F. D. Marks, and J. F. Gamache, 2000: Low-wavenumber structure and evolution of the hurricane inner core observed by airborne dual-Doppler radar. *Mon. Wea. Rev.*, **128**, 1653–1680.
- , M. D. Eastin, and J. F. Gamache, 2009: Rapidly intensifying Hurricane Guillermo (1997). Part I: Low-wavenumber structure and evolution. *Mon. Wea. Rev.*, in press.
- Schubert, W. H., 2004: A generalization of Ertel's potential vorticity to a cloudy, precipitating atmosphere. *Meteor. Z.*, **13**, 465–471.
- , M. T. Montgomery, R. K. Taft, T. A. Guinn, S. R. Fulton, J. P. Kossin, and J. P. Edwards, 1999: Polygonal eyewalls, asymmetric eye contraction, and potential vorticity mixing in hurricanes. *J. Atmos. Sci.*, **56**, 1197–1223.
- , S. A. Hausman, M. Garcia, K. V. Ooyama, and H.-C. Kuo, 2001: Potential vorticity in a moist atmosphere. *J. Atmos. Sci.*, **58**, 3148–3157.
- Terwey, W. D., and M. T. Montgomery, 2002: Wavenumber-2 and wavenumber-*m* vortex Rossby wave instabilities in a generalized three-region model. *J. Atmos. Sci.*, **59**, 2421–2427.
- Wang, Y., 2002a: Vortex Rossby waves in a numerically simulated tropical cyclone. Part I: Overall structure, potential vorticity, and kinetic energy budgets. *J. Atmos. Sci.*, **59**, 1213–1238.
- , 2002b: Vortex Rossby waves in a numerically simulated tropical cyclone. Part II: The role of tropical cyclone structure and intensity changes. *J. Atmos. Sci.*, **59**, 1239–1262.
- Yang, B., Y. Wang, and B. Wang, 2007: The effect of internally generated inner-core asymmetries on tropical cyclone potential intensity. *J. Atmos. Sci.*, **64**, 1165–1188.
- Yau, M. K., Y. Liu, D.-L. Zhang, and Y. Chen, 2004: A multiscale numerical study of Hurricane Andrew (1992). Part VI: Small-scale inner-core structures and wind streaks. *Mon. Wea. Rev.*, **132**, 1410–1433.